Brain, Behavior, & Immunity - Health 52 (2026) 101178

Contents lists available at ScienceDirect

Brain, Behavior, & Immunity - Health

journal homepage: www.editorialmanager.com/bbih/default.aspx

Macrostructural, microstructural, and cellular effects of neuroinflammation on the mouse brain

Yash Patel [a,b], Anita Woo [c,d], Sammy Shun Wai Shi [c,d], Eric Kim [a,d], Jean Shin [a,b], Yohan Yee [c,e], Jason P. Lerch [e,f], Brian J. Nieman [c,e], Tomas Paus [a,g], Zdenka Pausova [a,b,c,d,h,*]

[a] Centre Hospitalier Universitaire Sainte-Justine, University of Montreal, QC, Canada
[b] Department of Pediatrics, University of Montreal, Montreal, QC, Canada
[c] The Hospital for Sick Children, Translational Medicine Program, Toronto, ON, Canada
[d] Department of Physiology, University of Toronto, Toronto, ON, Canada
[e] Department of Medical Biophysics, University of Toronto, Toronto, ON, Canada
[f] Nuffield Department of Clinical Neurosciences, Oxford University, Oxford, United Kingdom
[g] Department of Psychiatry and Addictology and Department of Neuroscience, University of Montreal, QC, Canada
[h] Barcelonaβeta Brain Research Center, Barcelona, Spain

ARTICLE INFO

Keywords:
Neuroinflammation
Two-photon imaging of microglia
multimodal magnetic resonance imaging of the brain
In silico transcriptomics
Bioinformatics
PVALB inhibitory neuron
Layer 4,5 excitatory neuron
Cellular component of synapse

ABSTRACT

Neuroinflammation is increasingly implicated in post-infectious brain atrophy and cognitive impairment, as well as the etiology of neurodegenerative and psychiatric disorders. Here, we employed an established mouse model of neuroinflammation (systemic lipopolysaccharide [LPS]) and studied its macrostructural, microstructural, and cellular effects on the mouse brain. We combined whole-brain two-photon microscopy, multiparametric magnetic resonance imaging, and *in silico* transcriptomics. We demonstrate that LPS increases microglial soma size, a marker of microglial proinflammatory transformation, throughout the brain. LPS also induces *in vivo* volumetric increases of multiple brain regions, but not of the cerebral cortex. These *in vivo* increases are no longer observed *ex vivo* (post-fixation), suggesting they may be due to brain edema. Moreover, LPS induces microstructural alterations, as indicated by *ex vivo* reductions in fractional anisotropy and magnetization transfer ratio, which were most pronounced in the cerebral cortex. These reductions had the largest effect size in regions with higher expression of genes specific to parvalbumin inhibitory neurons and excitatory layer 4/5 intratelencephalic neurons, which were enriched in genes encoding synapse components. Thus, these results suggest that LPS-induced neuroinflammation may lead to brain edema, which spares the cerebral cortex, and microstructural alterations, which impact the cerebral cortex and may involve specific subtypes of inhibitory and excitatory neurons and their synapses.

1. Introduction

Neuroinflammation is a complex, multi-cellular process initiated by the activation of microglia, the resident immune cells in the brain (Waisman et al., 2015; Becher et al., 2016; Woodburn et al., 2021). Activated microglia release proinflammatory cytokines and reactive oxygen species, which affect the surrounding glial and neuronal cells (Becher et al., 2016; Glass et al., 2010). Neuroinflammation plays a critical role in post-infectious brain atrophy and cognitive impairment (Davis et al., 2023; Duggan et al., 2024) and the etiology of various neurodegenerative and psychiatric disorders, including Alzheimer's disease (Glass et al., 2010; Heneka et al., 2024) and depression (Miller et al., 2015; Troubat, 2021). Lipopolysaccharide (LPS), a potent endotoxin derived from gram-negative bacteria, is widely used to model neuroinflammation and its sequelae in the rodent and human brain (Robert et al., 2023; Marschallinger et al., 2020; Chen et al., 2012; Monzón-Sandoval, 2022; Lehnardt et al., 2003; Reichenberg et al., 2001).

Multiple effects of LPS-induced neuroinflammation on the brain have been reported (Robert et al., 2023; Marschallinger et al., 2020; Chen et al., 2012; Monzón-Sandoval, 2022; Lehnardt et al., 2003; Reichenberg et al., 2001), but a *comprehensive, whole-brain view* of its impacts on brain macrostructure, microstructure, and cellular underpinnings is still lacking. Multimodal magnetic resonance (MR) imaging coupled with

---

* Corresponding author. Department of Pediatrics, University of Montreal and Scientist, Centre Hospitalier Universitaire Sainte-Justine, Montreal, QC Canada.
E-mail address: zdenka.pausova@umontreal.ca (Z. Pausova).

https://doi.org/10.1016/j.bbih.2026.101178
Received 5 January 2026; Accepted 11 January 2026

microscopy and transcriptomics can provide such a view. Brain MR imaging can assess regional volumes (macrostructure) using anatomical T1-or T2-weighted imaging and microstructural variations using diffusion tensor imaging (DTI) and magnetization transfer (MT) imaging (Edwards et al., 2018). Both DTI and MT imaging are sensitive (but not specific) to water content and variations in the quantity and structure of cellular membranes, including those forming myelin and neurites (axons/dendrites/dendritic spines)(Edwards et al., 2018; Mori and Barker, 1999; Patel, 2020; Vavasour et al., 2011; Gareau et al., 2000; Sled, 2018; Uematsu et al., 2004). Additionally, brain MR images can be co-registered with *ex vivo* whole-brain two-photon microscopy images of various cell types, such as microglia, allowing the examination of regional perturbations of the cell types (Patel et al., 2024a; Amato et al., 2016). Further, brain MR images can be co-registered with *in silico* transcriptomic data, allowing for a further, albeit indirect, inference of cellular perturbations (Patel et al., 2020; Patel et al., 2024a; Patel et al., 2024b). This approach is implemented in 'virtual histology (Shin et al., 2018, 2023a; Patel et al., 2024c), a cell-type enrichment method integrating MR imaging data with independent bulk and single-nucleus RNA sequencing datasets from the mouse brain (Yao, 2021; Lein et al., 2007).

In the present study, we employed an established mouse model of neuroinflammation, specifically a 4-day series of intraperitoneal injections of 1 mg/kg/day LPS (Marschallinger et al., 2020; Chen et al., 2012), and a combination of whole-brain two-photon microscopy of microglia, multimodal MR imaging, and virtual histology. Our results revealed region-specific microglial remodelling, volume expansion, and alterations in brain microstructure involving synapse-related cellular components on specific subtypes of inhibitory and excitatory neurons. These results offer novel insights into the spatial dynamics and cellular underpinnings of LPS-induced neuroinflammation.

2. Results

A 4-day treatment regimen was conducted using 33 *Cx3cr1*$^{GFP/+}$ mice (20 weeks of age), assigned to either LPS ($n = 17$; 8 females, 9 males) or saline ($n = 16$; 8 females, 8 males) groups. In vivo T1-weighted imaging was acquired longitudinally (baseline and post-treatment). At the study endpoint, brains were perfused and fixed for *ex vivo* T2-weighted imaging, DTI, MT imaging, and whole-brain two-photon microscopy (serial two-photon tomography).

2.1. LPS-treated mice show widespread activation of microglia

Serial two-photon tomography of microglia, co-registered with T2-weighted MR imaging was used to quantify LPS-induced differences in microglial soma size (area) at the end of the 4-day treatment protocol. Microglial soma size is an established index of microglia proinflammatory transformation (Davis et al., 2017). Across the 22 atlas-based brain regions, LPS-treated mice exhibited a 6–16 % increase in microglial soma size compared to saline controls. This effect was most prominent in the midbrain ($\beta = 1.98$, p-value = 0.001, Fig. 1, Table S1a).

2.2. LPS induces hydrocephalus and regional brain edema

Longitudinal T1-weighted MR imaging was used to evaluate volumetric changes following LPS treatment, comparing pre- and post-intervention volumes. Globally, there was a 1.1 % increase in total brain volume (time*LPS interaction $\beta = 5.5$ mm^3, $p = 0.002$) in the LPS group, as compared with saline controls. This was driven in part by a 6 % volumetric enlargement of the ventricles (time*LPS interaction $\beta = 0.32$ mm^3, $p = 2.01E\text{-}07$). Similarly, several dorsal parenchymal regions, including the cerebellum, medulla, pons, midbrain, thalamus, and hypothalamus, showed 2–4 % volume increases in LPS-treated mice (all $p < 0.05$; Figs. 1 and 2, Table S2a). No statistically significant volumetric changes were observed in the cerebral cortex (all <1 %, $p > 0.05$, Fig. 2). In contrast, *ex vivo* imaging of perfusion-fixed brains revealed no volumetric differences (Fig. 1, Table S3). Given that post-fixation brains may shrink due to tissue water-loss during formaldehyde fixation (Wehrl et al., 2015; de Guzman et al., 2016), these *in vivo*-specific findings suggest that LPS induces accumulation of cerebrospinal fluid (CSF) in the ventricles (i.e., hydrocephalus) and regional parenchymal edema (Stokum et al., 2016). Furthermore, across all analyzed regions, the degree of parenchymal volume expansion correlated positively with the increase in microglial soma size (Pearson's $r = 0.50$, $p = 0.02$; Fig. S1).

2.3. LPS-treated mice show microstructural alterations in the cerebral cortex

We evaluated the Magnetization Transfer Ratio (MTR) and DTI-derived Fractional Anisotropy (FA) and Mean Diffusivity (MD) to assess microstructural integrity. LPS-treated mice displayed reduced MTR across multiple predominantly gray-matter regions. These reductions were most profound in the cerebral cortex, specifically within the temporal $\beta = -0.005$, $p = 3.17 \times 10^{-10}$), frontal ($\beta = -0.007$, $p = 3.82 \times 10^{-7}$), and parietal cortices ($\beta = -0.008$, $p = 7.55 \times 10^{-7}$) (Fig. 1, Table S4a). FA values were similarly reduced, with effects again most pronounced in the cerebral cortex (frontal $\beta = -0.026$, $p = 0.0001$) and cerebellar gray matter ($\beta = -0.031$, $p = 8.11E\text{-}05$, Fig. 1, Table S4a). No statistically significant differences in MD were observed between groups (Fig. 1, Table S4a).

2.4. Microstructural alterations in the cerebral cortex involve synapse-related cellular components on subtypes of inhibitory neurons and excitatory neurons

To understand better the cellular underpinnings of the LPS-induced microstructural changes (i.e., reductions in MTR and FA), we employed an *insilico, virtual histology* (Shin et al., 2018, 2023a; Patel et al., 2024c), approach. This cell-type enrichment analysis integrates MR imaging data with independent datasets of gene expression (bulk and single-nucleus RNA sequencing) in the mouse cortex (Yao, 2021; Lein et al., 2007). For this analysis, we utilized a 15-region cortical atlas based on the Allen Institute's Common Coordinate Framework (Fig. 3a). The effects of LPS on MTR, FA, and MD were retested across the 15 cortical regions of the atlas (Fig. 3a and b). The MTR and FA decreases (LPS vs. NaCl mice) were spatially correlated (Fig. 3c and d; $r = 0.58$, $p < 0.01$), with both exhibiting the largest effect sizes in the posterior parietal cortex (Fig. 3c and d).

To assess cell-type enrichment (and perform virtual histology (Shin et al., 2018; Shin et al., 2023a; Patel et al., 2024c)), the spatial correlation (across 15 cortical regions) between the bulk gene expression from the Allen Mouse Brain Atlas (Yao, 2021; Lein et al., 2007) and LPS-associated MTR (or FA) decreases (Fig. 3b) was tested against the cell-type specificity of individual genes (Fig. 3e). This analysis revealed that cortical regions with higher expression of genes specific to parvalbumin inhibitory neurons (INH_Pvalb) and excitatory layer 4/5 intratelencephalic neurons (EXC_L4/5_IT) show larger LPS-lowering effects on both MTR and FA (Fig. 3e). Functional gene ontology-enrichment analysis of these two sets of genes revealed enrichment in the cellular components of synapses (Fig. 3f). The enriched terms for the inhibitory INH_Pvalb neurons included 'axon terminus', 'internal component of synaptic membrane', and 'potassium channel complex', and the enriched terms for the excitatory EXC_L4/5_IT neurons included 'post-synaptic membrane' and 'dendritic spine' (Fig. 3f).

3. Discussion

The results of the present study suggest that systemic LPS induces: (i) widespread neuroinflammation (as evidenced by enlarged microglia soma size throughout the brain), (ii) hydrocephalus and edema of multiple brain regions, but not the cerebral cortex (as evidenced by *in vivo* [but not *ex vivo*] enlargement of ventricles and mostly dorsal,

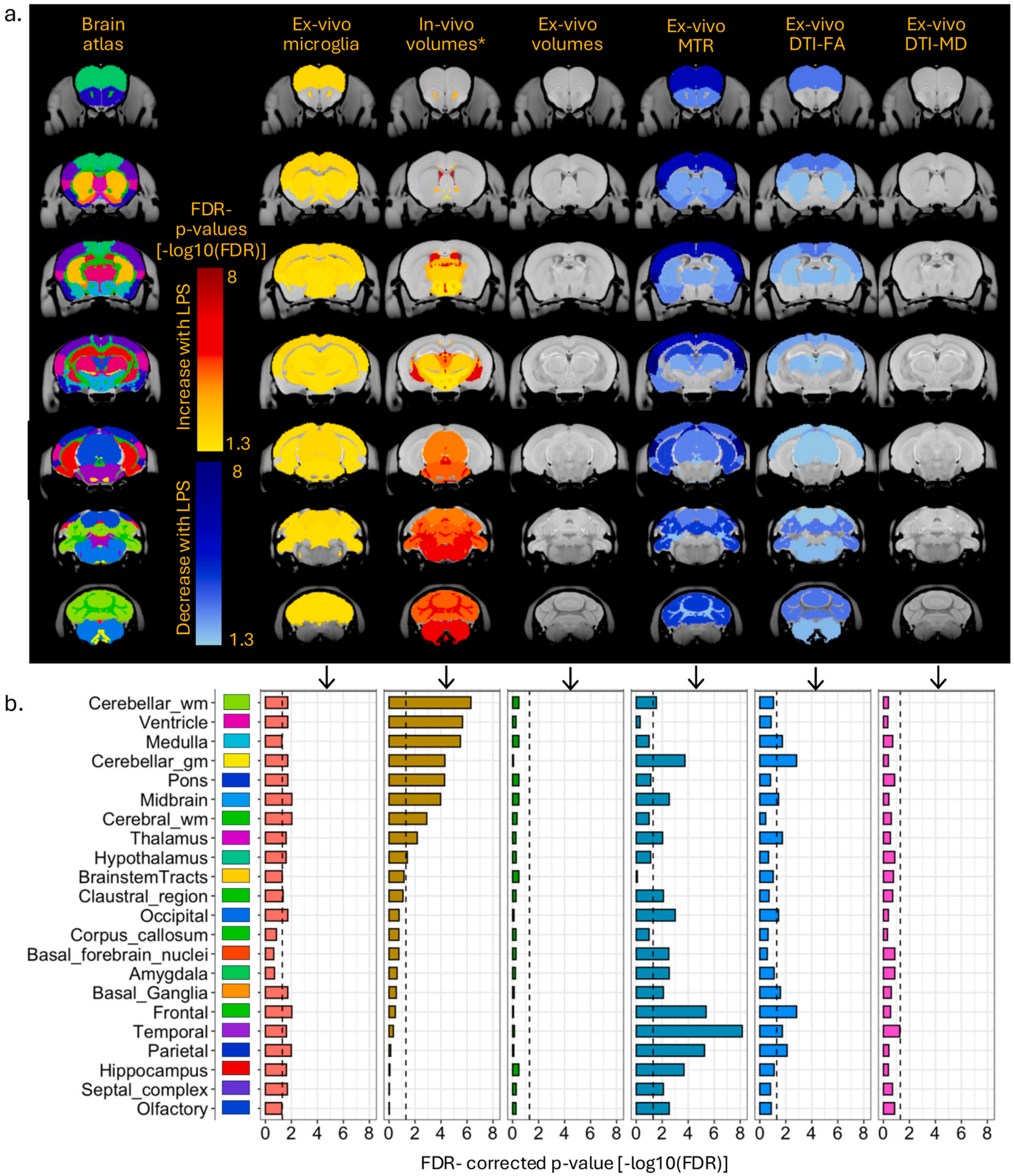

Fig. 1. Multi-modal, whole-brain characterization of LPS-induced neuroinflammation. (a) Coronal brain sections displaying the spatial distribution of False Discovery Rate (FDR)-corrected p-values projected onto the mouse anatomical atlas. Columns display (from left to right): the anatomical atlas, *ex vivo* microglial soma size (serial two-photon tomography), *in vivo* regional volume, *ex vivo* regional volume, and *ex vivo* microstructural MR imaging metrics (Magnetization Transfer Ratio [MTR], Fractional Anisotropy [FA], and Mean Diffusivity [MD]). (b) Corresponding region-wise bar plots illustrating the statistical significance of the LPS effect across 22 brain regions. The vertical dashed lines represent the threshold for statistical significance (FDR $p < 0.05$). Color Scale: The color bars indicate the direction and significance of the effect: warm colors (red/yellow) denote significant increases in the metric for LPS-treated mice relative to controls, while cool colors (blue/cyan) denote significant decreases. The scale represents the magnitude of significance (-log10(FDR-p value)), where higher values indicate stronger statistical significance. (For interpretation of the references to color in this figure legend, the reader is referred to the Web version of this article.)

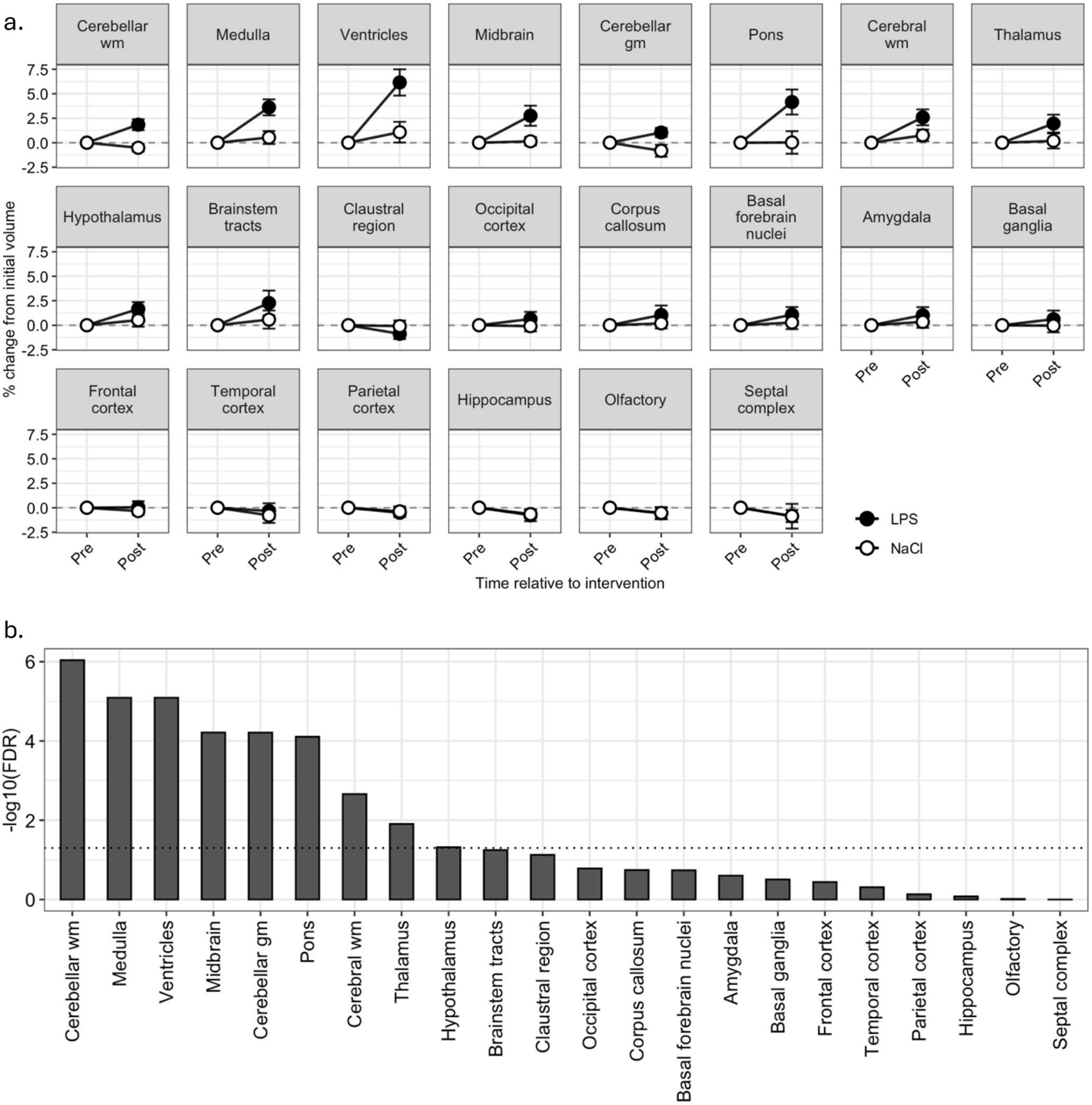

Fig. 2. Region-specific in vivo volumetric changes induced by LPS. (a) Longitudinal changes in regional brain volumes. Line plots display the mean percent change in volume from baseline (Pre) to post-treatment (Post) for LPS (black filled circles) saline mice (white open circles). Error bars represent the standard error of the mean (SEM). (b) Statistical significance from the cross-sectional analysis of group differences in regional volume between LPS and NaCl mice at timepoint 2 (post-treatment). Bars represent the -log10(FDR-adjusted p-value) for between-group comparisons in each region.

subcortical parenchymal regions), and (iii) microstructural alterations of mainly the cerebral cortex (as evidenced by lower MTR and FA in multiple regions of the cortex), possibly involving synapse-related cellular components on subtypes of inhibitory neurons and excitatory neurons (as inferred from *in silico* bulk and single cell RNAseq of the mouse cerebral cortex using cell-type and cellular components enrichment analysis).

Our combined use of *in vivo* and *ex vivo* (post-fixation) volumetric imaging revealed that LPS treatment induces hydrocephalus and edema in several, predominantly dorsal, parenchymal regions, but not in the cerebral cortex. These results support previous research demonstrating that LPS induces brain-fluid accumulation (Alexander et al., 2008; Cao et al., 2012; Kim, 2023) and ventricle enlargement (Robert et al., 2023), but they also provide new information on the regional distribution of this (likely) fluid accumulation. Regarding the underlying pathobiology, it has been demonstrated that systemic LPS disrupts the blood-brain barrier (Peng et al., 2021; Zou et al., 2022; Haruwaka et al., 2019), leading to intravascular fluid and protein leakage into the brain tissue and the development of vasogenic edema (Stokum et al., 2016). It has also been demonstrated that LPS enhances the production of CSF by the ventricular choroid plexus (Robert et al., 2023; Karimy et al., 2017), leading to the accumulation of CSF within the ventricles, i.e.,

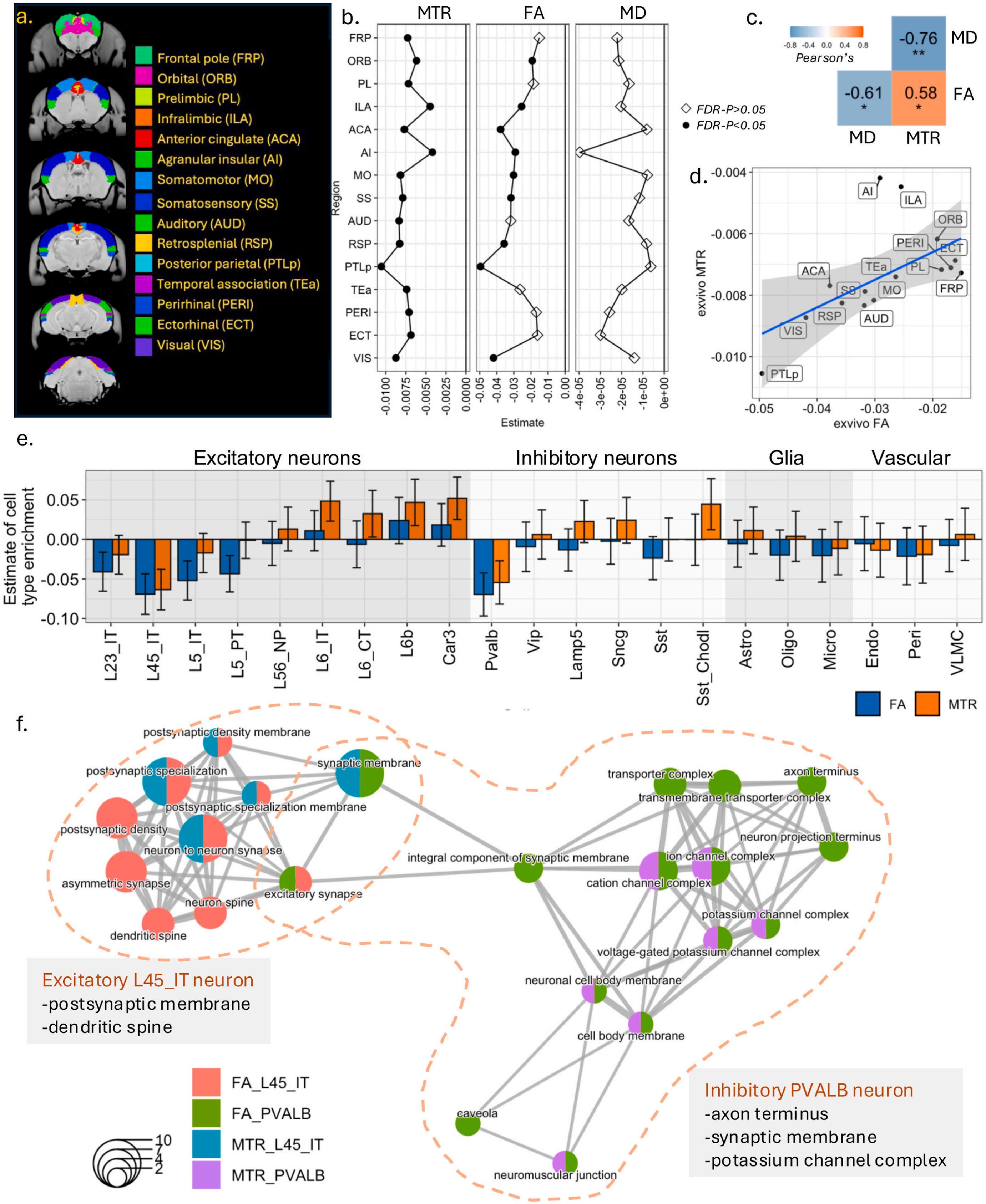

(caption on next page)

Fig. 3. Cerebral cortex-specific analysis of microstructural alterations (a) Coronal sections displaying the 15-region cortical parcellation derived from the Allen Mouse Brain Atlas used for analysis. Regions are color-coded with abbreviations listed on the right. (b) Regional estimates of the LPS effect (beta coefficients) on *ex vivo* Magnetization Transfer Ratio (MTR), Fractional Anisotropy (FA), and Mean Diffusivity (MD) across the 15 cortical regions. Filled circles indicate statistically significant effects. Filled circles represent FDR-adjusted $p < 0.05$. (c) Correlation matrix of LPS-induced changes across MTR, FA, and MD, spatially, across the 15 cortical regions. (d) Scatter plot demonstrating the coordinated effect of LPS on *ex vivo* MTR and FA across cortical regions. (e) Cell-type enrichment analysis based on correlations between MR imaging-derived LPS effect sizes (MTR, FA) and bulk tissue gene expression, across deciles of genes based on their cell specificity, using independently derived single-nucleus RNAseq data, and bulk tissue expression data. (f) Gene-ontology enrichment analysis of genes spatially correlated with LPS-induced MR imaging changes (MTR/FA) and expressed in L4/5 IT excitatory and parvalbumin (PVALB)-positive inhibitory neurons. Nodes represent significantly enriched cellular components, and edge thickness denotes the semantic similarity between GO terms. FRP: Frontal pole, ORB: Orbital, PL: Prelimbic, ILA: Infralimbic, ACA: Anterior cingulate, AI: Agranular insular, MO: Somatomotor, SS: Somatosensory, AUD: Auditory, RSP: Retrosplenial, PTLp: Posterior parietal, TEa: Temporal association, PERI: Perirhinal, ECT: Ectorhinal, VIS: Visual. (For interpretation of the references to color in this figure legend, the reader is referred to the Web version of this article.)

hydrocephalus (Robert et al., 2023). Accumulating CSF in the ventricles increases hydrostatic pressure within the ventricles, promoting a CSF shift outside to adjacent brain tissue and the development of interstitial edema (Stokum et al., 2016). The relative contributions of these two pathways to our findings are not clear. Further, other transient physiological mechanisms not assessed in this study, such as cerebral hyperemia or the expansion of perivascular spaces, could also have contributed to the *in vivo* volumetric changes. Future studies using *in vivo* quantitative MRI, such as T2 mapping or DTI-derived mean diffusivity, would be better suited to quantify changes in tissue water content directly.

We observed that regional increases in parenchymal volumes correlated positively with regional increases in microglial soma size ($r = 0.50$, $p = 0.02$; Fig. S1). Whether regions with higher microglia proinflammatory transformation are also regions with higher vulnerability to LPS-induced disruption of the blood-brain barrier and thus vasogenic edema requires further study. Of note, the observed increases in soma size are not likely to be a major contributor to the increases in parenchymal volumes, as (i) the enlargements in microglia soma size are generally accompanied by reductions in microglia neuropil, diminishing the overall cell volume (Davis et al., 2017), and (ii) microglia represent less than 5 % of all brain cells (Herculano-Houzel et al., 2006, 2011; Keller et al., 2018; Ero et al., 2018).

Our microstructural imaging showed that LPS treatment induces robust reductions in MTR and FA signals, predominantly in the cerebral cortex. The most affected region was the posterior parietal cortex. One previous study in rats also reported lower FA in LPS-treated animals compared to controls, which, similarly to our study, was most pronounced in the posterior parietal cortex (Kim, 2023). Prior research suggests that the MTR and FA signals in the cerebral cortex may be driven, to some extent, by macromolecules associated with dendritic arbor and spines (typically containing synapses) (Patel et al., 2019; Reveley et al., 2022). Our cell-type enrichment analysis supports this possibility. It shows that cortical regions with higher expression of genes specific to certain subtypes of excitatory and inhibitory neurons exhibit larger lowering effects of LPS on MTR and FA, and that these gene sets are enriched in the cellular components of dendritic spines and synapses. We speculate that the MTR and FA reductions may indicate a loss of synapse-related cellular components. Consistent with this possibility, previous research demonstrates that LPS lowers the expression of multiple inhibitory neuron genes (Rezaei et al., 2024), as well as the density and size of inhibitory neuron presynaptic puncta (Jung et al., 2023). The latter has been linked to the enhanced phagocytic function of microglia and their more frequent engulfment of inhibitory neuron synapses in LPS-treated animals compared to control animals (Jung et al., 2023). Neuronal hyperexcitability, linked to reduced GABAergic inhibition, has also been reported (Kurki et al., 2023). Our cell-type enrichment analysis suggests the involvement of both inhibitory and excitatory neurons, as well as the cellular components at inhibitory-excitatory neuron synapses (Fig. 3f). A loss of inhibition enhances neuron-toxic hyperexcitability. Accordingly, a previous study using MR spectroscopy of a brain region containing a large segment of the hippocampus shows that a single, larger dose of LPS (10 mg/kg) lowers N-acetyl aspartate/choline, creatine/choline, and myoinositol/choline ratios (Towner et al., 2018), indicating impaired neuronal health due to alterations in cellular membrane structure and cell bioenergetics (Towner et al., 2018). The subtypes of inhibitory and excitatory neurons implicated in this study were the parvalbumin inhibitory neurons and excitatory layer 4/5 intratelencephalic neurons (Fig. 3e). Parvalbumin inhibitory neurons are the largest subpopulation of cortical GABAergic neurons, which mediate lateral, feedforward, and feedback inhibition in local circuits and modulate the activity of excitatory neurons (Hijazi et al., 2023). The excitatory neurons within layer 4 are crucial for processing incoming sensory information. In contrast, the excitatory neurons within layer 5 are involved in cortical output, projecting to other cortical areas and subcortical structures. Parvalbumin inhibitory neurons are present in both layer 4 and layer 5[52–54].

In the present study, about half of all mice were females. Secondary sex-stratified analyses yielded comparable results for males and females regarding microglia soma size, MTR, and DTI metrics (Table S1b and S4b). The volumetric enlargements of parenchymal regions (but not of the ventricles) tended to be greater in females than in males (Table S2b and c). Previous research suggests this may be related to the effects of female sex hormones on tissue fluid retention and swelling (Stachenfeld et al., 1999; Farin et al., 2003).

The present study has some limitations. First, our *in vivo* longitudinal imaging used manganese chloride ($MnCl_2$) as a T1-weighted contrast agent. Although our protocol was standardized across groups and time points, we cannot rule out the possibility that $MnCl_2$ administration interfered with the LPS-induced inflammatory response. The use of $MnCl_2$ contrast is quite common in the literature on brain diseases due to its ability to enhance anatomical detail on T1 imaging. Future work using a $MnCl_2$-free *in vivo* arm would strengthen causal inference.

Second, our finding of *reduced* MTR in the cerebral cortex appears to contrast with human studies that reported *increased* magnetization transfer exchange rates (k_f) following acute inflammatory stimuli. For example, studies using a typhoid vaccine found *increases* in magnetization transfer (MT) metrics 3–4 h after the immune challenge (Plank et al., 2024; Harrison et al., 2015). These discrepancies are likely attributable to fundamental differences in experimental design. Thus, those studies measured the acute *in vivo* effects of inflammation, whereas our study assessed the cumulative impact of a 4-day LPS protocol using *ex vivo* imaging post-fixation. In addition, MTR – magnetization transfer ratio – is a simpler, composite, semi-quantitative metric (a ratio of images with and without a saturation pulse), and is influenced by acquisition parameters, B1 inhomogeneities, sequence timing, and tissue-relaxation times. In contrast, quantitative MT can assess more specific biophysical parameters such as the rate of the proton pool exchange. The differences in inflammatory timing (acute vs. sub-acute), imaging methods, and tissue state (*in vivo* vs. post-mortem) likely account for these opposing findings.

Third, our assessment of microglial proinflammatory transformation was based on soma size, an established morphological marker. We did not perform more comprehensive morphological analyses, such as Sholl analysis, branch length, or circularity, which can provide additional information on microglial proinflammatory transformation states (Leyh et al., 2021; Liu and Xiu, 2025). This is a methodological trade-off: our goal was a *whole-brain* characterization using serial two-photon tomography, which provides broad spatial coverage at the expense of the high-resolution detail needed for complex single-cell tracing (but with narrower spatial coverage).

Fourth, the *Cx3cr1GFP/+* mouse line used to identify microglia also labels other myeloid cells, including infiltrating peripheral monocytes. Given that our LPS model likely disrupted the blood-brain barrier, our serila two-photon tomography analysis could not definitively distinguish between resident microglia and infiltrating monocytes. Future work could use more specific markers to differentiate these cell populations.

Finally, our virtual histology, a cell-type enrichment analysis, correlates LPS-induced microstructural variations (MTR and FA reductions) with baseline gene-expression data from an external atlas. These external data are single-cell RNAseq data from the mouse cerebral cortex that can distinguish 21 cell types, including 7 subtypes of excitatory neurons, 5 subtypes of inhibitory neurons, 4 subtypes of glial cells (microglia, astrocytes, oligodendrocytes, and oligodendrocyte precursor cells), and 5 vascular cell subtypes. This *in silico* analysis does not directly measure changes in gene expression or cellular components in our own samples. It indicates that cortical regions with greater effects of LPS on MTR or FA show higher expression of genes specific to parvalbumin inhibitory and layer 4/5 excitatory neurons that are enriched in synaptic compartments. Therefore, the conclusion that these changes involve specific synaptic components on parvalbumin inhibitory and layer 4/5 excitatory neurons is an inference. However, this inference is biologically plausible and supported by previous research (Rezaei et al., 2024; Jung et al., 2023; Kurki et al., 2023). Notably, we did not detect significant reductions in MTR or FA in cerebral white matter, and our cortical virtual histology results did not implicate oligodendrocyte-enriched gene sets, suggesting that the observed microstructural effects in the cerebral cortex may not be primarily driven by myelin-related mechanisms. Prior reports of LPS-associated demyelination have largely focused on non-cortical contexts (Felts et al., 2005).

In summary, our findings provide a comprehensive, whole-brain view of LPS-induced neuroinflammation, evaluating region-specific microglial remodelling, volume expansions, and alterations in brain microstructure involving a loss of cellular components of inhibitory-excitatory neuron synapses. The findings may aid in the development of new diagnostic and treatment options for neuroinflammation, which is increasingly being recognized as one of the key contributors to the development of post-infectious brain atrophy and cognitive impairment, as well as neurodegenerative and psychiatric disorders (Glass et al., 2010; Davis et al., 2023; Duggan et al., 2024; Heneka et al., 2024; Miller et al., 2015; Troubat, 2021).

4. Methods

4.1. Animals

All MRI experiments were conducted on the *Cx3cr1*$^{GFP/GFP}$ mice (JAX stock #032127). At 20 weeks of age, mice were randomly assigned to receive either LPS (8 females and 9 males) or NaCl (8 females and 8 males). LPS (E. Coli strain O55:B5, Sigma Aldrich) was administered via intraperitoneal (i.p.) injection at a dose of 1 mg/kg of body weight daily for 4 consecutive days (or equivalent volume of 0.9 % NaCl). Throughout the 4 days, each cage received hydrogel, which is a hydration supplement, to ensure adequate hydration. The day before the first LPS injection (Time 1) and the day after the last LPS injection (Time 2), mice underwent an *in vivo* brain MR imaging. Mice were group-housed with up to 5 mice per cage and on a 12-h light/dark cycle with *ad* libitum access to food and water. Hormonal status was not tracked.

All animal procedures were performed in accordance and compliance with the Animals for Research Act of Ontario and the Canadian Council on Animal Care. The Centre for Phenogenomics Animal Care Committee approved all procedures performed on the animals (27–0341H).

4.2. In vivo longitudinal brain MR imaging

Image acquisition Before and after the 4-day treatment period, mice underwent *in vivo* T1-weighted FLASH 3D gradient echo manganese-enhanced magnetic resonance imaging (MEMRI) to assess region-specific macrostructural (volumetric) changes in the brain. To enhance the contrast of the images, 24 h before the scan, mice were i.p. injected with 0.4 mmol/kg of manganese chloride ($MnCl_2$; Sigma-Aldrich, Missouri, USA), which was administered in 2 equal doses to minimize the adverse effects of $MnCl_2$. A 7.0 T MRI scanner with a 30-cm diameter bore magnet (Bruker BioSpin, Ettlingen, Germany) was used to image the mice; up to 4 mice can be scanned in parallel using cryogenically cooled surface coils (Arbabi et al., 2022). The mice were anesthetized with 1–2 % isoflurane in 100 % oxygen, their respiration was monitored throughout the scan with self-gating signals (Nieman et al., 2009), and they were kept warm during the scan with a heated water platform. The imaging parameters for the *in vivo* MEMRI consisted of a 75-μm isotropic resolution was used with a T1-weighted FLASH 3D gradient echo sequence: TR = 26 msec, TE = 8.25 msec, flip angle = 23°, field-of-view = 25 x 22 × 22 mm, matrix = 334 x 294 x 294, 2 averages. The total scan duration was ~58 min, and the mice were allowed to recover in a heated chamber before returning to their home cage.

4.3. Ex vivo cross-sectional brain MR imaging

Image acquisition A multi-channel 7 T MR imaging scanner (Agilent Inc., Palo Alto, CA) was used to image perfusion-fixed brains in skulls.

Brain fixation After the completion of the 4-day LPS treatment, mice were anesthetized with a combination of Ketamine (150 mg/kg, Ketaset, TCP) and Xylazine (10 mg/kg, Rompun) at a dose of 0.1 mL/10g of body weight via *i.p.* injection. Once mice reached the proper plane of anesthesia, the chest cavity was opened, and the mice were intracardially perfused with 30 mL room-temperature solution of 0.1M phosphate-buffered solution (PBS) (Wisent, CAT: 311-010-CL) combined with 1 μL/mL heparin (10,000 USP/10 mL, Fresnius Kabi, DIN 02229066) and 2 mM ProHance® (Gadoteridol, Bracco Diagnostics Inc., DIN: 02229066) at a flow rate of 1.0 mL/min followed by 30 mL of room-temperature solution of 4 % paraformaldehyde (PFA) (EMS, Cederlane, Cat: 15710) combined with 2 mM ProHance® (Gadoteridol, Bracco Diagnostics Inc., DIN: 02229066) at a flow rate of 1.0 mL/min. Once the perfusion was complete, the skull (with brain inside) was removed and kept in 4 % PFA combined with 2 mM ProHance® (Gadoteridol, Bracco Diagnostics Inc., DIN: 02229066) for 1 day at 4 °C, which was then switched to 0.1M PBS combined with 2 mM ProHance® (Gadoteridol, Bracco Diagnostics Inc., DIN: 02229066) and 0.02 % sodium azide (Fisher, Cat: S227-10) at 4 °C for future *ex vivo* MR imaging. ProHance®, is a gadolinium-based MR imaging contrast agent used to enhance the *ex vivo* MR images. To obtain comparable inter-individual results for *ex vivo* MR imaging, the brains were allowed to equilibrate for at least 1 month before *ex vivo* MR imaging, as this ensures that the shrinkage of the brain is stabilized (de Guzman et al., 2016). Sixteen samples were imaged in parallel using a custom-built 16-coil solenoid array. Three sets of images were acquired: T2-weighted anatomical images were obtained with the following scanning parameters: T2-weighted 3D FSE cylindrical k-space acquisition sequence, TR/TE/ETL = 350 ms/12 ms/6, 2 averages, FOV/matrix-size = 20 x 20 × 25 mm/504 x 504 x 630. The resulting anatomical images had an isotropic resolution of 40-μm voxels. DTI scans were performed with the following scanning parameters: 30 directions, 5 b0 scans, b-value 2147 s/mm^2, TR 325 ms, echo spacing = 6 ms with first echo acquired 32 ms, followed by spacing of 6 ms for 6 echos. Resolution = 180 x 180 x 324 matrix, 78-μm isotropic voxels.

MTR images were obtained with the following scanning parameters: 224 x 224 x 278 matrix size, 90-μm isotropic, TR = 50 ms, TE = 2.8 msec, excitation flip angle = 54°, magnetization transfer (MT) flip pulse = 9000°, mt pulse width = 10 ms, Gaussian shape, spoiled gradient echo sequence. The total duration of the scanning session (T2-weighted, DTI, and MTR) was 14 h.

4.4. MR image processing

*In vivo*T1-weighted images and *ex vivo*T2-weighted images were processed using the same pipeline detailed below. The Mouse Brain Mapping (MBM) toolkit was used for intensity normalization and initial six-parameter linear (LSQ6) registration. The pre-processed T1/T2-weighted images were then segmented using the Multiple Automatically Generated Templates (MAGeT) Brain algorithm (Chakravarty et al., 2013). MAGeT-Brain employs a multi-atlas voting procedure based on a template library derived from the subject set. Segmentations from each atlas are propagated via image registration to a subset of the subject images (the 'template library') before being propagated to each subject image and fused. This approach leverages the neuroanatomical variability of the subjects to refine individual segmentations. These tools were implemented using the Pydpiper toolkit (Friedel et al., 2014). For this study, we used the Dorr_2008_Steadman _2013_Ullmann_2013_Richards_2011_Qiu_2016_Egan_2015 (Dorr et al., 2008; Steadman et al., 2014; Ullmann et al., 2013; Richards et al., 2011) mouse brain atlas to derive volumetric values for 22 regions, including 4 cortical lobar regions. DTI metrics (FA and MD) and MTR maps were registered to the *ex vivo* T2-weighted space using the Advanced Normalization Tools (ANTs) registration framework. The registration was performed using a series of transformations (Rigid, Affine, and SyN) with mutual information (MI) as the similarity metric, optimizing the alignment between the images. Segmented volume labels obtained from the MAGeT-Brain segmentation were used to extract mean FA, MD, and MTR values for each region of interest defined in the atlas.

All processed scans and registrations were visually inspected to ensure data quality and the accuracy of the registrations. Any scans exhibiting artifacts or misalignments were excluded from the analysis (n = 7 for DTI [FA, MD maps] and n = 6 for MTR).

4.5. Two-photon microscopy

Serial two-photon tomography of *Cx3cr1*$^{GFP/+}$ mice was used to assess microglia soma size; it was performed using a previously established system (Shigematsu et al., 2024; Kubota, 2014). Each brain was imaged at 1.37-μm in-plane resolution with 100-μm slice spacing, resulting in roughly 170 coronal slices and 8 h of imaging per brain. Signal intensities across samples were normalized using OpenCV tools (Stachenfeld et al., 1999). Contrast Limited Adaptative Histogram Equalization (CLAHE) was used to enhance local image contrast by distributing pixel intensities across a wider range of intensity values, thereby improving microglia conspicuity. Intensities were winsorized (scipy (Farin et al., 2003)) within a predetermined range to minimize the impact of intensity outliers on microglia detection and segmentation (lower bound threshold = 85 %, upper bound threshold = 0.5 %). Next, the normalized coronal sections were input for the 'fastCell' cell-segmentation pipeline, which employs an artificial neural network incorporating supervised machine learning to detect and segment individual cells (Plank et al., 2024). The neural network was trained using a set of manually segmented microglia labels (n ~ 8000) with varying size, shape, density, and signal intensity, from distinct samples and slices. The fastCell platform was used to train a neural network based on the ResNet-50 architecture, with a batch size of 16 and 20 epochs of training across two rounds. The first round used a learning rate (lr) of 1E-04, and the second round used 'lrs = slice (lr/1000, lr/10)', both rounds optimizing the Dice coefficient. The refined neural network was subsequently applied to segment the normalized coronal sections, generating output images that displayed segmented microglia labels throughout the brains. To verify the accuracy of the automated fastCell segmentation, we compared manual segmentation and fastCell counts of microglia across representative regions, including the cortex and hippocampus. Two-photon data were registered to *in vivo* MRI images using a two-step registration pipeline with ANTS (Karimy et al., 2017) and MNI-autoreg (Harrison et al., 2015) tools implemented within the Pydpiper toolkit (Haruwaka et al., 2019). First, a consensus average image of all two-photon images was created, which was then registered to native MR image space.

4.6. Statistical analyses

We performed two types of analyses: longitudinal and cross-sectional. The longitudinal analyses were performed with linear mixed-effects regression of *in vivo* T1-weighted images, where we have an image before and after the 4-day LPS treatment. We examined whether the LPS effect (LPS vs. NaCl) varied over Time (before and after the 4-day LPS treatment) by testing the LPS*Time interaction term, with sex as a fixed-effect covariate. P-values were false discovery rate (FDR)-corrected for 22 brain regions. For *ex vivo* volumes, FA, MD, MTR, and serial two-photon tomography-derived microglial soma sizes, we used linear regression to test the effect of LPS (vs. saline). For the serial two-photon tomography data, statistical models included the time difference between the time of sacrifice and the time to microscopy.

4.7. Virtual histology

To evaluate the relative cellular contributions to interregional variability in the effects of LPS on cortical MR imaging measures (FA and MTR), we developed a mouse analogous mouse approach based on previous methods designed for humans (Shin et al., 2018, 2023a; Patel et al., 2024c). For cell-type enrichment, we tested the relationship between a gene's cell-type specificity and the correlation between its expression level and the effect size of LPS-cortical MR imaging measure across the 15 cortical regions (Yao, 2021; Lein et al., 2007). To achieve this, we first use single-nucleus RNA sequencing data from the Allen Mouse Cortex (SMART-Seq) dataset (Yao, 2021), consisting of 59,150 isocortical cells (after excluding hippocampal samples), to determine the specificity for each gene to a given cell type (21 unique cell types: 7 subtypes of excitatory neurons, 5 subtypes of inhibitory neurons, 4 subtypes of glial cells [microglia, astrocytes, oligodendrocytes, and oligodendrocyte precursor cells], and 5 vascular subtypes). We calculate an aggregate measure of cell specificity using the CELLEX toolkit (Chakravarty et al., 2013). Cell specificity is defined as the mean of 4 different measures of specificity: gene enrichment score (Friedel et al., 2014), expression proportion, normalized specificity index (Steadman et al., 2014), and differential expression T-statistic, following rank normalization. Next, bulk-tissue *in situ hybridization* expression data from the Allen Mouse Brain Atlas were employed using the sagittal atlas. Mean gene expression was extracted from the Allen's mouse hierarchical atlas, mapped using their common atlas space, termed the Common Coordinate Framework, CCF (Wang et al., 2020). Lastly, we correlated the MR imaging-derived association effects of LPS on cortical metrics (FA and MTR) across the 15 cortical regions with mean gene expression across the same 15 cortical regions (also from the CCF). This expression-MR imaging profile correlation per gene was evaluated with decile-transformed gene specificity for each cell type using linear regression. We have described the method in detail previously (Patel et al., 2024a; Shin et al., 2023b). Finally, to characterize the functional relevance of genes driving the association between effects of LPS on MR imaging measures and expression of cell-type specific genes, we ran a Gene Ontology analysis using genes that were: (i) nominally significant $p < 0.05$ (MR imaging measure vs. gene expression correlation), and (ii) within the 10th decile in cell specificity for a given cell type (IT4/5 excitatory, or Parvalbumin inhibitory). The R library ClusterProfiler (Yu et al., 2012) was used to run gene ontology enrichment analysis and plot the results.

CRediT authorship contribution statement

Yash Patel: Formal analysis, Methodology, Writing – original draft. **Anita Woo:** Investigation, Writing – review & editing. **Sammy Shun Wai Shi:** Formal analysis, Investigation, Writing – review & editing. **Eric Kim:** Writing – review & editing. **Jean Shin:** Writing – review & editing. **Yohan Yee:** Methodology, Writing – review & editing. **Jason P. Lerch:** Funding acquisition, Methodology, Writing – review & editing. **Brian J. Nieman:** Methodology, Supervision, Writing – review & editing. **Tomas Paus:** Funding acquisition, Methodology, Writing – review & editing. **Zdenka Pausova:** Conceptualization, Funding acquisition, Supervision, Writing – review & editing.

Declaration of competing interest

The authors declare that they have no known competing financial interests or personal relationships that could have appeared to influence the work reported in this paper.

Acknowledgements

The present study was funded by the National Institutes of Health (R01AG056726). The authors wish to acknowledge the contribution of the Animal Resources and Imaging core services at The Centre for Phenogenomics for help with colony management, animal handling, and imaging.

Appendix A. Supplementary data

Supplementary data to this article can be found online at https://doi.org/10.1016/j.bbih.2026.101178.

Data availability

The authors do not have permission to share data.

References

Alexander, J.J., Jacob, A., Cunningham, P., Hensley, L., Quigg, R.J., 2008. TNF is a key mediator of septic encephalopathy acting through its receptor, TNF receptor-1. Neurochem. Int. 52, 447–456. https://doi.org/10.1016/j.neuint.2007.08.006.

Amato, S.P., Pan, F., Schwartz, J., Ragan, T.M., 2016. Frontiers | whole brain imaging with serial two-photon tomography. Front. Neuroanat. 10. https://doi.org/10.3389/fnana.2016.00031.

Arbabi, A., et al., 2022. Multiple-mouse magnetic resonance imaging with cryogenic radiofrequency probes for evaluation of brain development. Neuroimage 252, 119008. https://doi.org/10.1016/j.neuroimage.2022.119008.

Becher, B., et al., 2016. Cytokine networks in neuroinflammation. Nat. Rev. Immunol. 17 (1). https://doi.org/10.1038/nri.2016.123, 17 (2016-12-05).

Cao, C., et al., 2012. Hypertonic saline reduces lipopolysaccharide-induced mouse brain edema through inhibiting aquaporin 4 expression. Crit. Care 16, R186. https://doi.org/10.1186/cc11670.

Chakravarty, M.M., et al., 2013. Performing label-fusion-based segmentation using multiple automatically generated templates. Hum. Brain Mapp. 34, 2635–2654. https://doi.org/10.1002/hbm.22092.

Chen, Z., et al., 2012. Lipopolysaccharide-induced microglial activation and neuroprotection against experimental brain injury is independent of hematogenous TLR4. J. Neurosci. 32. https://doi.org/10.1523/JNEUROSCI.0730-12.2012.

Davis, B.M., Salinas-Navarro, M., Cordeiro, M.F., Moons, L., De Groef, L., 2017. Characterizing microglia activation: a spatial statistics approach to maximize information extraction. Sci. Rep. 7, 1576. https://doi.org/10.1038/s41598-017-01747-8.

Davis, H.E., McCorkell, L., Vogel, J.M., Topol, E.J., 2023. Long COVID: major findings, mechanisms and recommendations. Nat. Rev. Microbiol. 21, 133–146. https://doi.org/10.1038/s41579-022-00846-2.

de Guzman, A.E., Wong, M.D., Gleave, J.A., Nieman, B.J., 2016. Variations in post-perfusion immersion fixation and storage alter MRI measurements of mouse brain morphometry. Neuroimage 142, 687–695. https://doi.org/10.1016/j.neuroimage.2016.06.028.

Dorr, A.E., Lerch, J.P., Spring, S., Kabani, N., Henkelman, R.M., 2008. High resolution three-dimensional brain atlas using an average magnetic resonance image of 40 adult C57Bl/6J mice. Neuroimage 42, 60–69.

Duggan, M.R., et al., 2024. Proteomics identifies potential immunological drivers of postinfection brain atrophy and cognitive decline. Nat. Aging 4, 1263–1278. https://doi.org/10.1038/s43587-024-00682-4.

Edwards, L.J., Kirilina, E., Mohammadi, S., Weiskopf, N., 2018. Microstructural imaging of human neocortex in vivo. Neuroimage 182. https://doi.org/10.1016/j.neuroimage.2018.02.055.

Ero, C., Gewaltig, M.O., Keller, D., Markram, H., 2018. A cell atlas for the mouse brain. Front. Neuroinf. 12, 84. https://doi.org/10.3389/fninf.2018.00084.

Farin, A., Deutsch, R., Biegon, A., Marshall, L.F., 2003. Sex-related differences in patients with severe head injury: greater susceptibility to brain swelling in female patients 50 years of age and younger. J. Neurosurg. 98, 32–36. https://doi.org/10.3171/jns.2003.98.1.0032.

Felts, P.A., et al., 2005. Inflammation and primary demyelination induced by the intraspinal injection of lipopolysaccharide. Brain 128, 1649–1666.

Friedel, M., van Eede, M.C., Pipitone, J., Chakravarty, M.M., Lerch, J.P., 2014. Pydpiper: a flexible toolkit for constructing novel registration pipelines. Front. Neuroinf. 8, 67. https://doi.org/10.3389/fninf.2014.00067.

Gareau, P.J., Rutt, B.K., Karlik, S.J., Mitchell, J.R., 2000. Magnetization transfer and multicomponent T2 relaxation measurements with histopathologic correlation in an experimental model of MS. J. Magn. Reson. Imag. 11, 586–595. https://doi.org/10.1002/1522-2586(200006)11:6<586::aid-jmri3>3.0.co;2-v.

Glass, C.K., Saijo, K., Winner, B., Marchetto, M.C., Gage, F.H., 2010. Mechanisms underlying inflammation in neurodegeneration. Cell 140. https://doi.org/10.1016/j.cell.2010.02.016.

Harrison, N.A., et al., 2015. Quantitative magnetization transfer imaging as a biomarker for effects of systemic inflammation on the brain. Biol. Psychiatry 78, 49–57.

Haruwaka, K., et al., 2019. Dual microglia effects on blood brain barrier permeability induced by systemic inflammation. Nat. Commun. 10, 5816. https://doi.org/10.1038/s41467-019-13812-z.

Heneka, M.T., et al., 2024. Neuroinflammation in alzheimer disease. Nat. Rev. Immunol. 25 (5). https://doi.org/10.1038/s41577-024-01104-7, 25 (2024-12-09).

Herculano-Houzel, S., Mota, B., Lent, R., 2006. Cellular scaling rules for rodent brains. Proc. Natl. Acad. Sci. U. S. A. 103, 12138–12143. https://doi.org/10.1073/pnas.0604911103.

Herculano-Houzel, S., et al., 2011. Updated neuronal scaling rules for the brains of glires (rodents/lagomorphs). Brain Behav. Evol. 78, 302–314. https://doi.org/10.1159/000330825.

Hijazi, S., Smit, A.B., van Kesteren, R.E., 2023. Fast-spiking parvalbumin-positive interneurons in brain physiology and Alzheimer's disease. Mol. Psychiatr. 28, 4954–4967. https://doi.org/10.1038/s41380-023-02168-y.

Jung, H., et al., 2023. LPS induces microglial activation and GABAergic synaptic deficits in the hippocampus accompanied by prolonged cognitive impairment. Sci. Rep. 13, 6547. https://doi.org/10.1038/s41598-023-32798-9.

Karimy, J.K., et al., 2017. Inflammation-dependent cerebrospinal fluid hypersecretion by the choroid plexus epithelium in posthemorrhagic hydrocephalus. Nat. Med. 23, 997–1003. https://doi.org/10.1038/nm.4361.

Keller, D., Ero, C., Markram, H., 2018. Cell densities in the mouse brain: a systematic review. Front. Neuroanat. 12, 83. https://doi.org/10.3389/fnana.2018.00083.

Kim, E., et al., 2023. Mapping acute neuroinflammation in vivo with diffusion-MRI in rats given a systemic lipopolysaccharide challenge. Brain Behav. Immun. 113. https://doi.org/10.1016/j.bbi.2023.07.010.

Kubota, Y., 2014. Untangling GABAergic wiring in the cortical microcircuit. Curr. Opin. Neurobiol. 26, 7–14. https://doi.org/10.1016/j.conb.2013.10.003.

Kurki, S.N., et al., 2023. Acute neuroinflammation leads to disruption of neuronal chloride regulation and consequent hyperexcitability in the dentate gyrus. Cell Rep. 42, 113379. https://doi.org/10.1016/j.celrep.2023.113379.

Lehnardt, S., et al., 2003. Activation of innate immunity in the CNS triggers neurodegeneration through a toll-like receptor 4-dependent pathway. Proc. Natl. Acad. Sci. U. S. A. 100, 8514–8519. https://doi.org/10.1073/pnas.1432609100.

Lein, E.S., et al., 2007. Genome-wide atlas of gene expression in the adult mouse brain. Nature 445, 168–176.

Leyh, J., et al., 2021. Classification of microglial morphological phenotypes using machine learning. Front. Cell. Neurosci. 15, 701673.

Liu, R., Xiu, J., 2025. 3D imaging and pathological analysis of microglia in LPS-treated mice with light-sheet fluorescence microscopy. J. Neuroimmunol. 399, 578525.

Marschallinger, J., et al., 2020. Lipid-droplet-accumulating microglia represent a dysfunctional and proinflammatory state in the aging brain. Nat. Neurosci. 23 (2). https://doi.org/10.1038/s41593-019-0566-1, 23 (2020-01-20).

Miller, A.H., Raison, C.L., Miller, A.H., Raison, C.L., 2015. The role of inflammation in depression: from evolutionary imperative to modern treatment target. Nat. Rev. Immunol. 16 (1). https://doi.org/10.1038/nri.2015.5, 16 (2015-12-29).

Monzón-Sandoval, J., et al., 2022. Lipopolysaccharide distinctively alters human microglia transcriptomes to resemble microglia from Alzheimer's disease mouse models. Dis. Model. Mech. 15. https://doi.org/10.1242/dmm.049349.

Mori, S., Barker, P.B., 1999. Diffusion magnetic resonance imaging: its principle and applications. Anat. Rec. 257. https://doi.org/10.1002/(SICI)1097-0185(19990615)257:3<102::AID-AR7>3.0.CO;2-6.

Nieman, B.J., Szulc, K.U., Turnbull, D.H., 2009. Three-dimensional, in vivo MRI with self-gating and image coregistration in the mouse. Magn. Reson. Med. 61, 1148–1157. https://doi.org/10.1002/mrm.21945.

Patel, Y., et al., 2019. Maturation of the human cerebral cortex during adolescence: Myelin or dendritic arbor? Cerebr. Cortex 29, 3351–3362. https://doi.org/10.1093/cercor/bhy204.

Patel, Y., et al., 2020. Virtual histology of multi-modal magnetic resonance imaging of cerebral cortex in young men. Neuroimage 218. https://doi.org/10.1016/j.neuroimage.2020.116968.

Patel, Y., et al., 2024a. Obesity and the cerebral cortex: underlying neurobiology in mice and humans. Brain Behav. Immun. 119, 637–647. https://doi.org/10.1016/j.bbi.2024.04.033.

Patel, Y., et al., 2024b. Genetic risk factors underlying white matter hyperintensities and cortical atrophy. Nat. Commun. 15 (1). https://doi.org/10.1038/s41467-024-53689-1, 15 (2024-11-04).

Patel, Y., et al., 2024c. Obesity and the cerebral cortex: underlying neurobiology in mice and humans. Brain Behav. Immun. 119, 637–647. https://doi.org/10.1016/j.bbi.2024.04.033.

Peng, X., Luo, Z., He, S., Zhang, L., Li, Y., 2021. Blood-brain barrier disruption by lipopolysaccharide and sepsis-associated encephalopathy. Front. Cell. Infect. Microbiol. 11, 768108. https://doi.org/10.3389/fcimb.2021.768108.

Plank, J.R., et al., 2024. Detection of neuroinflammation induced by typhoid vaccine using quantitative magnetization transfer MR: a randomized crossover study. J. Magn. Reson. Imag. 59, 1683–1694.

Reichenberg, A., et al., 2001. Cytokine-associated emotional and cognitive disturbances in humans. Arch. Gen. Psychiatry 58, 445–452. https://doi.org/10.1001/archpsyc.58.5.445.

Reveley, C., et al., 2022. Diffusion MRI anisotropy in the cerebral cortex is determined by unmyelinated tissue features. Nat. Commun. 13 (1). https://doi.org/10.1038/s41467-022-34328-z, 13 (2022-11-05).

Rezaei, S., Prevot, T.D., Vieira, E., Sibille, E., 2024. LPS-induced inflammation reduces GABAergic interneuron markers and brain-derived neurotrophic factor in mouse prefrontal cortex and hippocampus. Brain Behav. Immun. Health 38, 100761. https://doi.org/10.1016/j.bbih.2024.100761.

Richards, K., et al., 2011. Segmentation of the mouse hippocampal formation in magnetic resonance images. Neuroimage 58, 732–740.

Robert, S.M., et al., 2023. The choroid plexus links innate immunity to CSF dysregulation in hydrocephalus. Cell 186, 764–785 e721. https://doi.org/10.1016/j.cell.2023.01.017.

Shigematsu, N., Miyamoto, Y., Esumi, S., Fukuda, T., 2024. The anterolateral barrel subfield differs from the posteromedial barrel subfield in the morphology and cell density of parvalbumin-positive GABAergic interneurons. eNeuro 11. https://doi.org/10.1523/ENEURO.0518-22.2024.

Shin, J., et al., 2018. Cell-specific gene-expression profiles and cortical thickness in the human brain. Cerebr. Cortex 28, 3267–3277. https://doi.org/10.1093/cercor/bhx197.

Shin, J., Patel, Y., Parker, N., Paus, T., Pausova, Z., 2023a. Prediabetic HbA1c and cortical atrophy: underlying neurobiology. Diabetes Care 46, 2267–2272. https://doi.org/10.2337/dc23-1105.

Shin, J., Patel, Y., Parker, N., Paus, T., Pausova, Z., 2023b. Prediabetic HbA1c and cortical atrophy: underlying neurobiology. Diabetes Care dc231105.

Sled, J.G., 2018. Modelling and interpretation of magnetization transfer imaging in the brain. Neuroimage 182, 128–135. https://doi.org/10.1016/j.neuroimage.2017.11.065.

Stachenfeld, N.S., Silva, C., Keefe, D.L., Kokoszka, C.A., Nadel, E.R., 1999. Effects of oral contraceptives on body fluid regulation. J. Appl. Physiol. 87, 1016–1025. https://doi.org/10.1152/jappl.1999.87.3.1016.

Steadman, P.E., et al., 2014. Genetic effects on cerebellar structure across mouse models of autism using a magnetic resonance imaging atlas. Autism Res. 7, 124–137.

Stokum, J.A., Gerzanich, V., Simard, J.M., 2016. Molecular pathophysiology of cerebral edema. J. Cerebr. Blood Flow Metabol. 36, 513–538. https://doi.org/10.1177/0271678X15617172.

Towner, R.A., et al., 2018. Assessing long-term neuroinflammatory responses to encephalopathy using MRI approaches in a rat endotoxemia model. GeroScience 40, 49–60. https://doi.org/10.1007/s11357-018-0009-z.

Troubat, R., et al., 2021. Neuroinflammation and depression: a review. Eur. J. Neurosci. 53. https://doi.org/10.1111/ejn.14720.

Uematsu, H., et al., 2004. Magnetization transfer micro-MR imaging of live excised lamprey spinal cord: characterization and immunohistochemical correlation. AJNR Am. J. Neuroradiol. 25, 1816–1820.

Ullmann, J.F.P., Watson, C., Janke, A.L., Kurniawan, N.D., Reutens, D.C., 2013. A segmentation protocol and MRI atlas of the C57BL/6J mouse neocortex. Neuroimage 78, 196–203.

Vavasour, I.M., Laule, C., Li, D.K., Traboulsee, A.L., MacKay, A.L., 2011. Is the magnetization transfer ratio a marker for myelin in multiple sclerosis? J. Magn. Reson. Imag. 33, 713–718. https://doi.org/10.1002/jmri.22441.

Waisman, A., Liblau, R.S., Becher, B., 2015. Innate and adaptive immune responses in the CNS. Lancet Neurol. 14. https://doi.org/10.1016/S1474-4422(15)00141-6.

Wang, Q., et al., 2020. The Allen mouse brain common coordinate framework: a 3D reference atlas. Cell 181. https://doi.org/10.1016/j.cell.2020.04.007.

Wehrl, H.F., et al., 2015. Assessment of murine brain tissue shrinkage caused by different histological fixatives using magnetic resonance and computed tomography imaging. Histol. Histopathol. 30, 601–613. https://doi.org/10.14670/HH-30.601.

Woodburn, S.C., et al., 2021. The semantics of microglia activation: neuroinflammation, homeostasis, and stress. J. Neuroinflammation 18 (1). https://doi.org/10.1186/s12974-021-02309-6, 18 (2021-11-06).

Yao, Z., et al., 2021. A taxonomy of transcriptomic cell types across the isocortex and hippocampal formation. Cell 184. https://doi.org/10.1016/j.cell.2021.04.021.

Yu, G., Wang, L.-G., Han, Y., He, Q.-Y., 2012. clusterProfiler: an R package for comparing biological themes among gene clusters. OMICS A J. Integr. Biol. 16, 284–287.

Zou, P., et al., 2022. Lipopolysaccharide downregulates the expression of ZO-1 protein through the akt pathway. BMC Infect. Dis. 22, 774. https://doi.org/10.1186/s12879-022-07752-1.